12. A. M. Ganan-Calvo, J. M. Gordillo, *Phys. Rev. Lett.* **87**, 274501 (2001).
13. P. Garstecki, H. A. Stone, G. M. Whitesides, *Phys. Rev. Lett.* **94**, 164501 (2005).
14. P. Garstecki, M. J. Fuerstman, H. A. Stone, G. M. Whitesides, *Lab Chip* **6**, 437 (2006).
15. P. Guillot, A. Colin, *Phys. Rev. E* **72**, 066301 (2005).
16. F. P. Bretherton, *J. Fluid Mech.* **10**, 166 (1961).
17. W. Engl, M. Roche, A. Colin, P. Panizza, A. Adjari, *Phys. Rev. Lett.* **95**, 208304 (2005).
18. D. R. Link, S. L. Anna, D. A. Weitz, H. A. Stone, *Phys. Rev. Lett.* **92**, 054503 (2004).
19. P. Garstecki, M. A. Fischbach, G. M. Whitesides, *Appl. Phys. Lett.* **86**, 244108 (2005).
20. S. R. Hodges, O. E. Jensen, J. M. Rallison, *J. Fluid Mech.* **501**, 279 (2004).
21. H. Wong, C. J. Radke, S. Morris, *J. Fluid Mech.* **292**, 95 (1995).
22. Fig. S1 details the design of the microfluidic network.
23. Materials and methods are available as supporting material on *Science* Online.
24. This work was supported by the U.S. Department of Energy under award DE-FG02 OOER45852. P.G. thanks the Foundation for Polish Science for financial support. We thank the Harvard Center for Nanoscale Systems for the use of microfabrication facilities and the fast cameras.

Microfluidic Bubble Logic

Manu Prakash* and Neil Gershenfeld

We demonstrate universal computation in an all-fluidic two-phase microfluidic system. Nonlinearity is introduced into an otherwise linear, reversible, low–Reynolds number flow via bubble-to-bubble hydrodynamic interactions. A bubble traveling in a channel represents a bit, providing us with the capability to simultaneously transport materials and perform logical control operations. We demonstrate bubble logic AND/OR/NOT gates, a toggle flip-flop, a ripple counter, timing restoration, a ring oscillator, and an electro–bubble modulator. These show the nonlinearity, gain, bistability, synchronization, cascadability, feedback, and programmability required for scalable universal computation. With increasing complexity in large-scale microfluidic processors, bubble logic provides an on-chip process control mechanism integrating chemistry and computation.

Microfluidic "lab-on-a-chip" devices, where picoliters of fluids can be precisely manipulated in microscopic channels under controlled reaction conditions, have revolutionized analytical chemistry and biosciences. Recent advances in elastomeric pneumatic microvalves (*1*) and large-scale integration (*2*) have enabled complex process control for a wide variety (*3*, *4*) of applications in single-phase microreactors. However, pneumatic elastomeric microvalves require external macroscopic solenoids for their operation, and cascadability and feedback (where a signal acts on itself) are currently lacking in microfluidic control architectures.

Several reaction chemistries have been implemented in segmented-flow two-phase microreactors, where individual nanoliter droplets traveling inside microchannels are used as reaction containers (*5*, *6*). Dielectrophoretic (*7*) and electrostatic (*8*) schemes have been proposed for on-chip droplet management, but these require external control of individual gates. Devices that exploit the dynamics of droplets inside microchannels would make high-throughput screening and combinatorial studies possible (*9*), but passive techniques (*10*, *11*) have not provided control over individual droplets.

We demonstrate bubble logic that implements universal Boolean logic in physical fluid dynamics. This provides a droplet-level, internal, inherently digital flow control mechanism

Center for Bits and Atoms, Massachusetts Institute of Technology, Cambridge, MA 02139, USA.

*To whom correspondence should be addressed. E-mail: manup@mit.edu

for microfluidic processors. A bubble traveling in a microchannel can represent a bit of information as well as carry a chemical payload, making it possible to integrate chemistry with computation for process control. Bubble logic preserves the information representation from input to output; thus, devices can be cascaded, allowing implementation of combinatorial and sequential Boolean logic. A bubble can be transported to a desired location in a complex microfluidic network via a series of logic gates corresponding to an equivalent Boolean circuit.

Logic gates have been implemented chemically in chemical concentration waves in a Belousov-Zhabotinsky reaction (*12*) and in DNA (*13*). Purely hydrodynamic fluidic logic (*14*) was used to build a trajectory controller, an all-fluidic display, nondestructive memory, and a simple computer (*15*). Because the high Reynolds numbers required for inertial interactions cannot be maintained in the microscopic geometries needed for higher operating speeds and increasing integration, fluids with non-Newtonian polymer additives have been used to realize a constant flow source and a bistable gate (*16*, *17*). Boolean logic in a single-phase Newtonian fluid was implemented by changes in flow resistance (*18*), but because its input and output representation were not the same, these devices could not be cascaded. Bubble logic, based on hydrodynamic bubble-to-bubble interactions, is more similar in bit representation to theoretical billiard ball logic (*19*) based on the elastic collision of particles, and to magnetic bubble memory (*20*) relying on interactions of magnetic domains in garnet films. These schemes all conserve infor-

mation, because during a logic operation a bit is neither created nor destroyed.

The pressure-driven flow of bubbles in an interconnected microfluidic network can be described with a simplified dynamic flow resistance model (*21*). Single-phase flow resistance of a channel at low Reynolds number can be approximated as $\Delta p/Q \propto \mu L/h^3 w$, where $\Delta p/LQ$ is defined as the hydraulic resistance per unit length, μ is the dynamic viscosity, and h and w are the height and width of the microchannel. The pressure drop due to a long bubble flowing in a channel, where the bubble radius in an unbounded fluid is greater than the channel width and the continuous phase completely wets the channel surface, is nonlinear and is proportional to $\Delta p \propto \sigma/w(3Ca^{2/3})$, where Ca is the capillary number ($Ca = \mu u/\sigma$), u is the flow velocity of the continuous phase, and σ is the surface tension between liquid and gas phase (*22*, *23*). For small flow rates, this increased flow resistance is primarily due to viscous dissipation in the thin film of liquid surrounding the bubble. With the presence of surfactant molecules on the air-water interface, viscous dissipation in the lubrication film further increases as a result of the no-slip boundary conditions at the interface. In this case, the pressure drop across a finite-length bubble is also linearly dependent on the bubble length until it reaches a critical value, beyond which it is constant (*24*). When a bubble traveling in a microchannel arrives at a bifurcation with low capillary number (where the bubble does not split because surface tension dominates the viscous stress), it chooses the branch with highest instantaneous flow (*25*, *26*).

With an increased flow resistance due to the presence of a bubble in a microchannel, flow lines in surrounding interconnected channels can be perturbed. The nonlinearity in such a system arises from the introduction of interfacial force terms from the boundary conditions due to the presence of a free surface at the fluid interfaces (*27*). These nonlinear time-dependent interactions are the basis of our bubble logic gates. In the implementation described here, we used water as the liquid medium [with added surfactant 2% (w/w) Tween 20 to stabilize the interfaces] and nitrogen bubbles. Planar bubble logic devices were fabricated in poly(dimethyl siloxane) (PDMS) by single-layer soft lithography and plasma bonding to Pyrex substrates.

Figure 1 (top row; see also movie S1) shows an AND/OR bubble logic gate that evaluates both AND (·) and OR (+) simultaneously, as is necessary to satisfy bit conservation. As shown in the center column, the first bubble arriving at the junction always enters A+B (the wider channel, with less resistance), increasing the output flow resistance of A+B and thus directing a bubble arriving later to A·B. The time trace plotted for all four channels shows that the two bubbles interact only if they arrive within a window τ_0 (for this gate $\tau_0 \sim 0.5$ ms at flow rate $Q = 0.25$ μl/s) determined by the residence time of the bubble in the gate geometry.

Fan-out for the output signal from one gate to act as an input signal for multiple gates can be implemented by splitting bubbles at a T junction (25), requiring restoration of the bubble size. Figure 1 (bottom row; see also movie S2) demonstrates a universal $\overline{A}\cdot B$ gate, which implements a NOT and AND with gain so that a smaller bubble can switch a larger one. There are two counteracting asymmetries: an input channel with an asymmetric T junction (bottom), and a narrow stream of injected flow from the control channel (top) into the wider of the two bifurcations. By introducing a bubble into the control channel, injected side flow can be dynamically turned on and off, thereby enabling control of the direction of flow of the output bubble arriving at the bifurcation (bottom row, center column). The change in injected flow from the control channel (ΔQ) when a bubble passes through is nonlinearly related to the size of the bubble, providing gain as plotted in Fig. 1 (bottom row, right column) against the dimensionless bubble size (bubble length/channel width).

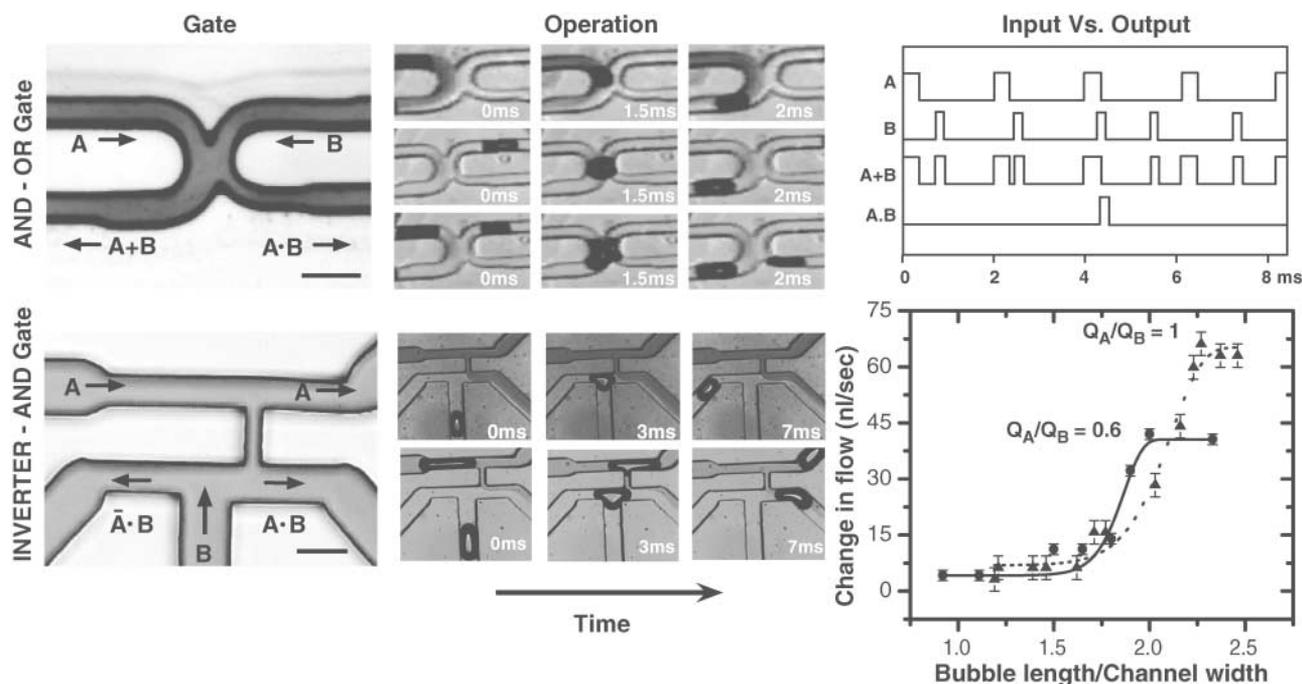Segmented-flow reactors often operate at kilohertz frequencies, where the limiting factor

Fig. 1. Universal microfluidic bubble logic. The top row shows a two-input AND-OR gate. The channel height is 70 μm; scale bar, 100 μm. With a water flow rate of 0.25 μl/s and nitrogen bubbles with a pressure of 0.5 psi, the gate propagation delay is 2 ms. The bottom row depicts a universal $\overline{A}\cdot B$ gate with gain that can be used to switch a larger bubble by a smaller one. For the bubbles shown, the ratio of the size of the input to the control is 1.2, and the graph shows the nonlinear dependence of the inlet flow on the control bubble size for two ratios of the control to the inlet flow rate.

Fig. 2. Bistability. (**A** to **F**) Toggling of a flip-flop memory; with a water flow rate of 0.25 μl/s, the switching time is 8 ms. The channel height is 70 μm; scale bar, 100 μm. (**G**) Change in free surface energy (31) for the toggle (solid line) and stored (dashed line) bubbles during switching. (**H**) Flip-flops cascaded to form a ripple counter.
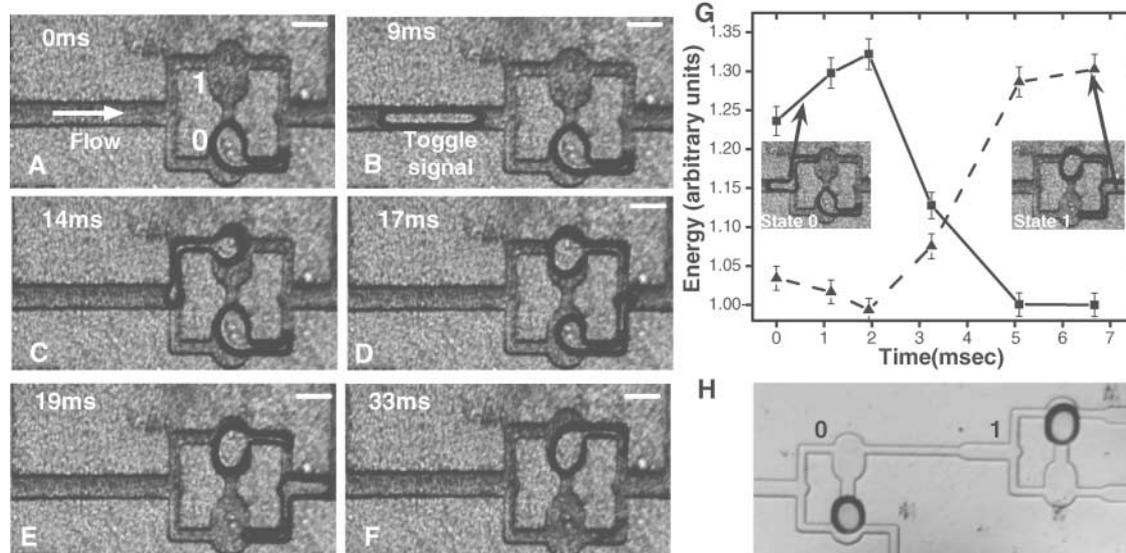
for high-throughput screening is the rate of information extraction from individual droplets. We present a bistable mechanism (Fig. 2 and movie S3) capable of on-demand trapping and release of individual bubbles, implemented as a 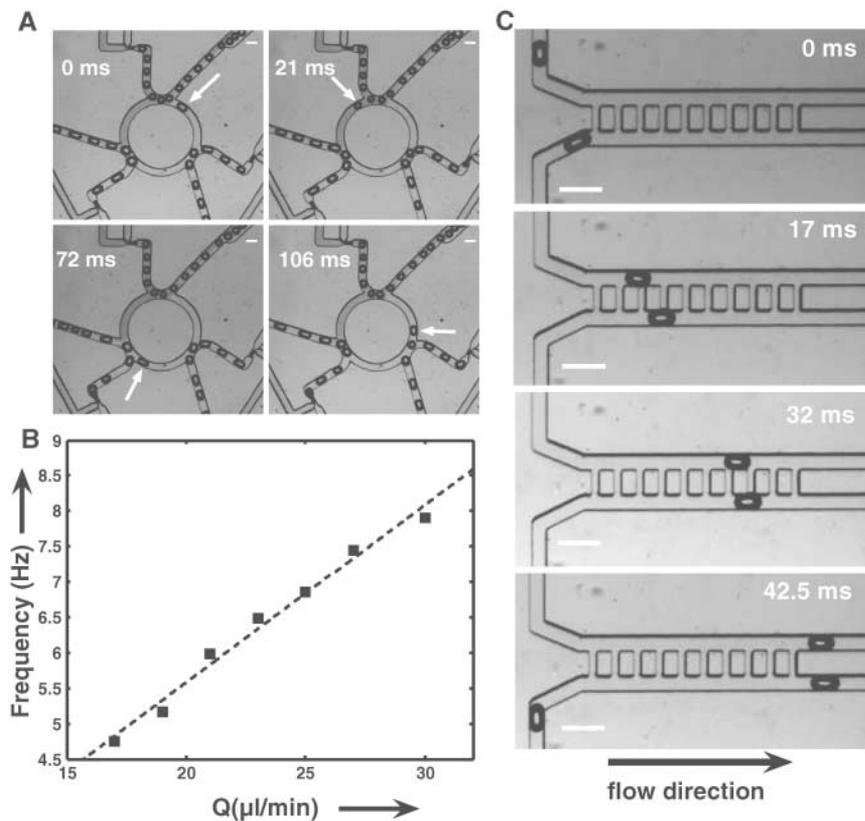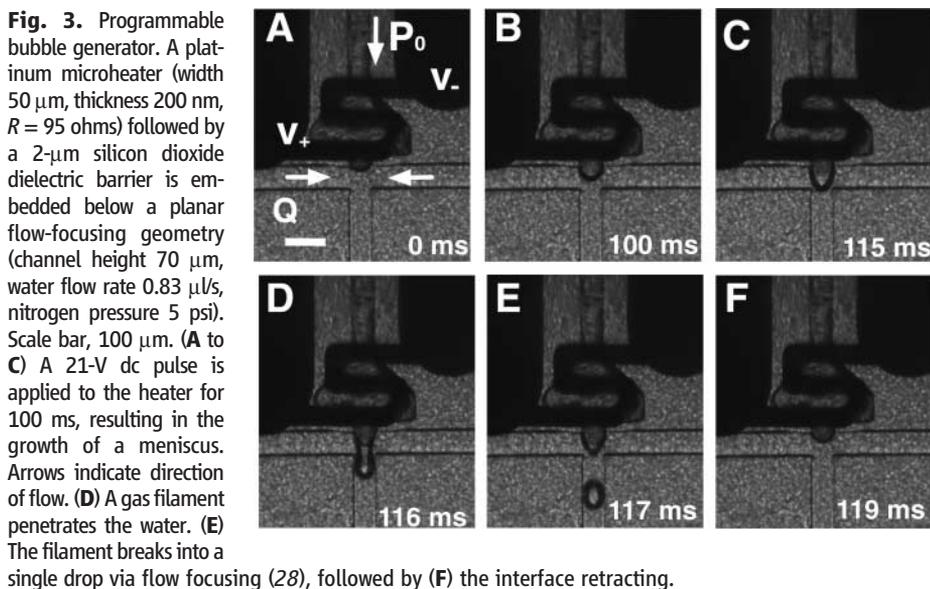flip-flop memory. A bubble minimizes its surface energy by adopting a shape with the smallest surface area. The flip-flop geometry (Fig. 2A) presents an incoming bubble with two elliptical lobes where the surface energy of the bubble is at a minimum, as shown in the plot of energy versus time (Fig. 2G and fig. S1A). The device holds a single bubble indefinitely until it is toggled by another bubble arriving at the inlet, dislodging the stored bubble by flow through the channel connecting the lobes. Although the incoming bubbles are much longer than the Rayleigh-Plateau criteria for breakup (25), the presence of a bubble in the flip-flop ensures that the incoming bubble travels to a single lobe without breakup (the bifurcation diagram is plotted in fig. S1B and the repeatability in the time trace in fig. S1C). We have used this mechanism to implement a bistable flow switch (fig. S2), with a switching time an order of magnitude less than that for comparable macroscopic elements such as solenoid valves (1), as well as a cascaded ripple counter (Fig. 2H).

To provide an electronic interface to bubble logic devices, we developed a thermal electro–bubble modulator (Fig. 3 and movie S4) capable of generating bubbles on demand synchronized to an electric pulse. Methods for high-frequency continuous production of monodisperse microbubbles and droplets in microfluidic devices have been extensively studied (27–29). Electrogeneration of on-demand single aqueous droplets (30) requires high on-chip electric fields on the order of ~1 kV. Our thermal electro–bubble generator uses an integrated microheater and modified flow-focusing geometry (Fig. 3), enabling operation at a much lower voltage (21 V). For the case of pressure-driven flow (Fig. 3A), there is a static balance at the air-water interface $\Delta P + \tau_v = Ca^{-1}k$ (29), where ΔP is the difference in pressure, τ_v is the viscous stress, and k represents the mean curvature. An applied temperature pulse reduces the surface tension σ at the air-water interface, allowing a gas filament to penetrate the liquid (Fig. 3D), which breaks to form a single bubble (Fig. 3E).

A standard test of cascadability and feedback in a new logic family is steady-state operation of a ring oscillator. We implemented this with three identical AND gates connected via three delay lines in a ring structure (Fig. 4A and movie S5) with constant-frequency T-junction bubble generators at the inputs. A bubble propagating around the ring delay line (Fig. 4A, arrow) increases the resistance of the outgoing channel when it arrives at the input of one of the three AND gates, generating a pressure pulse that launches another bubble in response. The oscillation frequency of this device can be written as $f \propto 1/[3(l/v + \tau_d)]$, where f is the oscillator frequency, l is the length of the delay line, v is the mean velocity of the bubble traveling in the delay line, and τ_d is the propagation delay of the AND gate. This frequency can be tuned by increasing the flow rate of the continuous phase (Fig. 4B).

The operation of bubble logic requires the relative arrival of bubbles at a gate to be within a transit time; scalability requires restoration of relative timing errors. We achieved this via a planar fluidic resistance ladder network. This geometry (Fig. 4C and movie S6) places inter-

Fig. 3. Programmable bubble generator. A platinum microheater (width 50 μm, thickness 200 nm, R = 95 ohms) followed by a 2-μm silicon dioxide dielectric barrier is embedded below a planar flow-focusing geometry (channel height 70 μm, water flow rate 0.83 μl/s, nitrogen pressure 5 psi). Scale bar, 100 μm. (**A** to **C**) A 21-V dc pulse is applied to the heater for 100 ms, resulting in the growth of a meniscus. Arrows indicate direction of flow. (**D**) A gas filament penetrates the water. (**E**) The filament breaks into a single drop via flow focusing (28), followed by (**F**) the interface retracting.

Fig. 4. Feedback, cascadability, and synchronization. (**A**) Three AND gates connected as a ring oscillator, with constant-frequency bubble generators at the inputs. A bubble arriving at the input delay line releases one at the output delay line. Scale bar, 100 μm. (**B**) Dependence of the oscillation frequency on the flow rate Q. (**C**) A fluidic ladder network for timing restoration. With a flow rate of 0.5 μl/s, a restoration of ~10 ms is achieved over a span of ~40 ms. Scale bar, 100 μm.

connecting fluid channels (continuous-phase flow resistance *r*) between two data-carrying channels (continuous-phase flow resistance *R*, with *r* > *R*). A single bubble traversing the ladder is slowed down by flow through the alternate path. When both bubbles are present simultaneously, there is a net flow from the channel with the leading bubble to the one with the lagging bubble, creating a relative velocity gradient until the bubbles are synchronized (fig. S3).

Because bubble logic chips have no moving parts, they can be fabricated in a wide variety of materials, including silicon and glass, that are compatible with reaction chemistries unsuitable for PDMS channels. Moreover, because they operate at low Reynolds and capillary numbers, further reduction in size is feasible with faster switching times. The device mechanisms do not depend on non-Newtonian fluid properties; hence, matching dimensionless flow parameters will allow bubble logic circuits to be designed using different fluids, such as water droplets in oil or oil droplets in water.

The universal logic gates, toggle flip-flop, ripple counter, synchronizer, ring oscillator, and electro–bubble modulator presented here exhibit nonlinearity, bistability, gain, synchronization, cascading, feedback, and programmability. Having shown the required properties of a scalable logic family, they can be used to create complex microfluidic circuits capable of performing arbitrary fluid process control and computation in an integrated fashion. Such circuits may re- duce the size, cost, and complexity of current microfluidic systems, thereby enabling the development of very-large-scale microfluidic reactors for use in areas including combinatorial chemistry and drug discovery. These bubble logic processors, where a bit of information can also carry a chemical payload, merge chemistry with computation.

References and Notes

1. M. A. Unger, H.-P. Chou, T. Thorsen, A. Scherer, S. R. Quake, *Science* **288**, 113 (2000).
2. T. Thorsen, S. J. Maerkl, S. Quake, *Science* **298**, 580 (2002); published online 26 September 2002 (10.1126/science.1076996).
3. C. C. Lee *et al.*, *Science* **310**, 1793 (2005).
4. F. K. Balagaddé, L. You, C. L. Hansen, F. H. Arnold, S. R. Quake, *Science* **309**, 137 (2005).
5. K. Jensen, A. Lee, *Lab Chip* **4**, 31N (2004).
6. B. Zheng, L. S. Roach, R. F. Ismagilov, *J. Am. Chem. Soc.* **125**, 11170 (2003).
7. P. R. C. Gascoyne *et al.*, *Lab Chip* **4**, 299 (2004).
8. D. Link *et al.*, *Angew. Chem. Int. Ed.* **45**, 2556 (2006).
9. M. Joanicot, A. Ajdari, *Science* **309**, 887 (2005).
10. Y.-C. Tan, J. S. Fisher, A. I. Lee, V. Cristini, A. P. Lee, *Lab Chip* **4**, 292 (2004).
11. G. Cristobal, J.-P. Benoit, M. Joanicot, A. Ajdari, *Appl. Phys. Lett.* **89**, 034104 (2006).
12. O. Steinbock, P. Kettunen, K. Showalter, *J. Phys. Chem.* **100**, 18970 (1996).
13. G. Seelig, D. Soloveichik, D. Y. Zhang, E. Winfree, *Science* **314**, 1585 (2006).
14. A. Conway, *A Guide to Fluidics* (Macdonald, London, 1972).
15. C. A. Belsterling, *Fluidic Systems Design* (Wiley Interscience, New York, 1971).
16. A. Groisman, M. Enzelberger, S. R. Quake, *Science* **300**, 955 (2003).
17. A. Groisman, S. R. Quake, *Phys. Rev. Lett.* **92**, 094501 (2004).
18. T. Vestad, D. W. Marr, T. Munakata, *Appl. Phys. Lett.* **84**, 5074 (2004).
19. E. Fredkin, T. Toffoli, *Int. J. Theor. Phys.* **21**, 219 (1982).
20. H. Chang, Ed., *Magnetic Bubble Technology: Integrated-Circuit Magnetics for Digital Storage and Processing* (IEEE Press, New York, 1975).
21. F. Jousse, G. Lian, R. Janes, J. Melrose, *Lab Chip* **5**, 646 (2005).
22. F. P. Bretherton, *J. Fluid Mech.* **10**, 166 (1961).
23. H. Wong, C. Radke, S. Morris, *J. Fluid Mech.* **292**, 95 (1995).
24. C. W. Park, *Phys. Fluids* **4**, 2335 (1992).
25. D. Link, S. Anna, D. Weitz, H. Stone, *Phys. Rev. Lett.* **92**, 054503 (2004).
26. M. J. Fuerstman, P. Garstecki, G. M. Whitesides, *Science* **315**, 828 (2007); published online 4 January 2007 (10.1126/science.1134514).
27. T. Thorsen, R. W. Roberts, F. H. Arnold, S. R. Quake, *Phys. Rev. Lett.* **86**, 4163 (2001).
28. P. Garstecki *et al.*, *Appl. Phys. Lett.* **85**, 2649 (2004).
29. T. Ward, M. Faivre, M. Abkarian, H. Stone, *Electrophoresis* **26**, 3716 (2005).
30. M. He, J. S. Kuo, D. T. Chiu, *Appl. Phys. Lett.* **87**, 031916 (2005).
31. Surface energy for a bubble trapped in a channel was evaluated from photomicrographs captured by a high-speed camera (Phantom V5.0, Vision research, minimum exposure time 10 μs). The grayscale images from the camera were digitized, a threshold filter was applied, and an edge detector was used to locate the bubbles and find their perimeter.
32. Supported by the MIT Center for Bits and Atoms (NSF grant CCR-0122419).

Chemical and Spectroscopic Evidence for an Fe^V-Oxo Complex

Filipe Tiago de Oliveira,[1]* Arani Chanda,[1]* Deboshri Banerjee,[1] Xiaopeng Shan,[2] Sujit Mondal,[1] Lawrence Que Jr.,[2]† Emile L. Bominaar,[1]† Eckard Münck,[1]† Terrence J. Collins[1]†

Iron(V)-oxo species have been proposed as key reactive intermediates in the catalysis of oxygen-activating enzymes and synthetic catalysts. Here, we report the synthesis of [Fe(TAML)(O)]$^-$ in nearly quantitative yield, where TAML is a macrocyclic tetraamide ligand. Mass spectrometry, Mössbauer, electron paramagnetic resonance, and x-ray absorption spectroscopies, as well as reactivity studies and density functional theory calculations show that this long-lived (hours at −60°C) intermediate is a spin $S = 1/2$ iron(V)-oxo complex. Iron-TAML systems have proven to be efficient catalysts in the decomposition of numerous pollutants by hydrogen peroxide, and the species we characterized is a likely reactive intermediate in these reactions.

High-valent iron-oxo intermediates are used in biological systems to carry out challenging oxidations in many scenarios (*1–3*). It has long been known that heme-based systems, biological as well as synthetic, do not attain the iron(V) state. Rather, the so-called "Compound I" intermediate involves the Fe^{IV}(oxo)(porphyrin-radical-cation), Fe^{IV}(O)(P$^{+\bullet}$), which is well established in peroxidases and catalases and presumed with considerable justification to be the reactive oxidizing species of the cytochrome P450s (*1*). Recently, Newcomb and co-workers reported laser flash photolysis experiments of an iron-corrole complex (*4*) and cytochrome P450 mutant CYP 119 (*5*), in which optically detected transients were tentatively assigned to Fe^V-oxo species. Que and co-workers, on the basis of ^{18}O labeling experiments, have postulated that an HO-Fe^V-oxo oxidant is an intermediate in the large family of Rieske dioxygenase enzymes (*3*). Iron(V) complexes are exceedingly rare, but recently, Wieghardt and co-workers reported spectroscopic evidence for a non-heme $S = 1/2$ iron(V)-nitrido complex produced by photolysis of an azidoiron(III) precursor (*6*).

Tetraamido macrocyclic ligands (TAMLs) can stabilize a variety of high-valent iron complexes, including a high-spin ($S = 2$) iron(IV) complex, intermediate-spin ($S = 1$) iron(IV) complexes, oxo-bridged diiron(IV) dimers, and an $S = 1$ iron(III)(TAML-radical-cation) complex [all reviewed in (*7*)]. The structurally characterized oxo-bridged complex, [(Fe^{IV}B*)$_2$(μ-oxo)]$^{2-}$, **2**, (B*, a TAML, is shown in Fig. 1) was obtained by reacting the monomeric iron(III) precursor, [Fe^{III}B*(H$_2$O)]$^-$, **1**, with air (*8*). Fe-TAML activation of peroxide has been shown to be useful in numerous applications (*9, 10*). The deprotonated TAML (a tetraanion) presents the iron with four exceptionally strong amido-*N* σ-donors. Therefore, it has been reasonable to expect (*11*) that this macrocyclic ligand would be capable of stabilizing an oxo-iron(V) complex when an Fe^{III}(TAML) complex is treated with an oxygen-atom transfer agent such as peroxide. A variety of iron(IV) complexes have been synthesized by reacting iron(II) precursors with oxygen donors

[1]Department of Chemistry, Carnegie Mellon University, Pittsburgh, PA 15213, USA. [2]Department of Chemistry and Center for Metals in Biocatalysis, University of Minnesota, Minneapolis, MN 55455, USA.

*These authors contributed equally to this work.
†To whom correspondence should be addressed. E-mail: que@chem.umn.edu (L.Q.); eb7g@andrew.cmu.edu (E.L.B.); emunck@cmu.edu (E.M.); tc1u@andrew.cmu.edu (T.J.C.)